Automatica 140 (2022) 110219

Contents lists available at ScienceDirect

Automatica

journal homepage: www.elsevier.com/locate/automatica

Lyapunov-based damping controller with nonlinear MPC control of payload position for a knuckle boom crane ☆

Geir Ole Tysse *, Andrej Cibicik, Lars Tingelstad, Olav Egeland

Department of Mechanical and Industrial Engineering, Norwegian University of Science and Technology (NTNU), N-7491 Trondheim, Norway

ARTICLE INFO

Article history:
Received 23 October 2019
Received in revised form 24 October 2021
Accepted 17 January 2022
Available online xxxx

Keywords:
Crane control
Energy-based control
Nonvanishing perturbation
Nonlinear model predictive control

ABSTRACT

A crane control system is proposed where the crane payload follows a desired position trajectory with ultimately bounded pendulum motion. The proposed control system includes a Lyapunov-based damping controller, which stabilizes the dynamics of the payload by increasing the damping of the pendulum motion. The crane with the resulting stabilized dynamics is controlled with a tracking controller based on NMPC (nonlinear model predictive controller). The Lyapunov-based damping controller is designed so that the stabilized closed-loop pendulum dynamics are exponentially stable. This means that the pendulum motion is ultimately bounded in the presence of bounded perturbations. The control variables of the NMPC tracking controller are constrained so that the perturbations to the damping controller are sufficiently bounded. The resulting system tracks the desired payload position with bounded pendulum motion. The control system is validated in simulations and experiments using a scaled laboratory version of a knuckle boom crane.

1. Introduction

Cranes are essential in a wide range of operations in offshore and onshore industries. Cranes are required to transfer payloads to a desired location without excessive payload oscillations. Payload oscillations are typically caused by crane motion, and may cause danger and interruption of crane activities. The use of automatic control has therefore been introduced to reduce downtime and improve the efficiency and safety of crane operations. The research community has devoted much effort to this, and both open-loop and closed-loop methods have been developed.

Early research on crane control was presented in Sakawa and Nakazumi (1985) where a combination of a state observer and a linear optimal controller was used for a rotary crane. Comprehensive reviews are found in Abdel-Rahman et al. (2003) and Ramli et al. (2017). An important research field for cranes is the measurement of payload motion, which is considered in Rauscher et al. (2018).

Input shaping is an open-loop technique which has been studied extensively for cranes (Blackburn et al., 2010; Cutforth & Pao, 2004), where the goal is to generate trajectories that will not induce pendulum oscillation. This was achieved by using a flatness approach in Knierim et al. (2010), where sufficiently smooth trajectories of the payload were generated for feedback control, and a simple dynamical system could be derived so that a controller could be derived by pole placement. In addition, the acceleration from the proposed controller was converted to velocity inputs for the drives of the trolley and winch. This was further developed in Rauscher et al. (2018). Flatness-based control of a gantry crane for transferring a payload between two positions with minimum transition time was proposed in Kolar et al. (2017).

Several controllers based on neural networks and fuzzy logic have been proposed for cranes. A combination of a learning strategy and adaptive control method was proposed in Qian et al. (2017) for an offshore boom crane.

Nonlinear energy-based controllers of 2-DOF overhead crane systems were proposed in Fang et al. (2001) by using LaSalle's invariance principle, and in Chung and Hauser (1995) where the stability was analyzed about a desired periodic orbit. In Yu et al. (1995) a nonlinear tracking controller was proposed for a 2-DOF gantry crane system using a singular perturbation design. An energy-based feedback controller was presented in Sun et al. (2013) for 4-DOF overhead cranes. The proposed controller was derived by considering practical input constraints, and achieved satisfactory trolley displacements while damping out payload

☆ The research presented in this paper was funded by the Norwegian Research Council, SFI Offshore Mechatronics, Project Number 237896. The material in this paper was partially presented at the 18th European Control Conference, June 25–28, 2019, Naples, Italy. This paper was recommended for publication in revised form by Associate Editor Antonella Ferrara under the direction of Editor Thomas Parisini.

* Corresponding author.
E-mail addresses: geir.o.tysse@ntnu.no (G.O. Tysse), andrej.cibicik@ntnu.no (A. Cibicik), lars.tingelstad@ntnu.no (L. Tingelstad), olav.egeland@ntnu.no (O. Egeland).

https://doi.org/10.1016/j.automatica.2022.110219

oscillations. A Lyapunov-based nonlinear controller for a 3-DOF cart and payload system with constrained pendulum length and trolley stroke was proposed in Yoshida (1998). In Sun et al. (2015) the authors proposed an energy-based controller by using Barbalat's lemma for the position of a trolley with hoisting while suppressing payload oscillation in one plane. A nonlinear controller using a feedback linearization technique was proposed in Wu and He (2016). In Cibicik et al. (2018) a controller based on LaSalle's invariance principle was designed to damp out oscillations of a bifilar pendulum. In Sun et al. (2016) the authors presented an adaptive controller which was designed to damp payload oscillations and to reduce unexpected overshoots for the jib slew and trolley movements for a tower crane system.

In Wu et al. (2015) the authors proposed model predictive control (MPC) for a 2-DOF trolley and payload system. In Vukov et al. (2012) a nonlinear MPC was designed to optimize point to point motion with varying pendulum length for a cart and winch mechanism. A controller based on an MPC and a particle swarm optimizer for an overhead crane was proposed in Smoczek and Szpytko (2017). The particle swarm optimizer was used for limiting the residual swinging of the payload. A hybrid feedforward and MPC controller was proposed in Kimiaghalam et al. (2001) for damping the pendulum motion in one plane of a ship-mounted crane with a Maryland rigging system. In Arnold et al. (2005) the authors proposed a real-time MPC, where the nonlinear model was linearized along a reference trajectory, to control the luffing and slewing motion of a mobile harbor crane. This work is further developed in Neupert et al. (2010) where exact linearization and input/output linearization were used to simplify the nonlinear behavior of the system, and by adding a linearized feedforward part and a stabilizing feedback part.

In this paper we propose a control system with a Lyapunov-based damping controller which stabilizes the pendulum dynamics of the crane payload. This Lyapunov-based controller is designed so that it can be combined with a tracking controller which is used to control the position of the crane tip and the cable length. The goal of the Lyapunov-based controller is to stabilize the pendulum dynamics so that the design of the tracking controller is simplified. The tracking controller is a nonlinear MPC (NMPC) controller. The NMPC controller can be designed with a lower sampling frequency and with less computational complexity due to the stabilized dynamics. In particular, the NMPC do need not damp the oscillations of the pendulum, which makes the NMPC problem sufficiently simple to be run in real time.

The Lyapunov-based controller is designed so that the unperturbed pendulum system is exponentially stable. This means that the pendulum motion is ultimately bounded in the presence of a bounded perturbation (Khalil, 2002). The NMPC is then designed so that the control action of the tracking controller is a bounded perturbation to the pendulum dynamics. The crane tip and cable length can then track a reference trajectory with ultimately bounded pendulum motion. The performance of the controller is studied in simulations and in experiments using a scaled laboratory version of a knuckle boom crane. A preliminary version of the proposed control system was published in the conference paper (Tysse & Egeland, 2019). The extensions of this paper are that the crane tip moves also in the vertical direction, the cable length is controlled, and experimental validation is included.

The rest of this work is organized as follows. The kinematics and dynamics of the crane and the payload are presented in Section 2. Then the control strategy is explained in Section 3. The Lyapunov-based damping controller is presented in Section 4, and the nonlinear MPC controller is presented in Section 5. Simulation and experimental validation are presented in Section 6, and finally, conclusions are presented in Section 7.

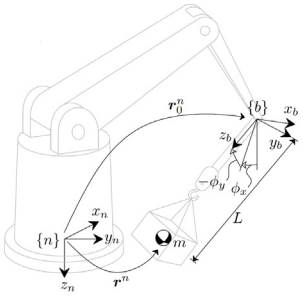

(a) Spherical pendulum and suspension point system with payload mass and length of pendulum L. The origin of frame b is fixed at the suspension point, while the origin of frame n is a non-moving frame located inside the crane king.

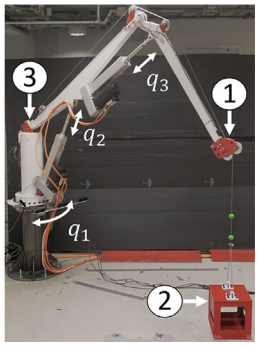

(b) A small-scale knuckle boom crane with suspension point (1), crane payload (2) and slewing actuator (3).

Fig. 1. The knuckle boom crane.

2. Modeling

2.1. Crane payload kinematics

We consider a knuckle boom crane with a hoisting mechanism (Fig. 1(a)). The crane tip is the suspension point of the hoisting line, which is a massless cable with length L. The payload is a point mass m. The inertial frame n has the z axis pointing vertically downwards, and a frame b is fixed in the suspension point with the z axis along the cable. The rotation matrix from n to b is

$$\boldsymbol{R}_b^n = \boldsymbol{R}_x(\phi_x)\boldsymbol{R}_y(\phi_y), \tag{1}$$

where $\boldsymbol{R}_x$ and $\boldsymbol{R}_y$ are the rotation matrices about the x and y axes (Siciliano et al., 2008). The generalized coordinates of the payload are given by $\boldsymbol{q}_1 = [\phi_x, \phi_y]^{\mathrm{T}}$. Coordinate vectors are given in the frame indicated by the trailing superscript, which means that, e.g., $\boldsymbol{r}^n = \boldsymbol{R}_b^n \boldsymbol{r}^b$.

The position of the suspension point is $\boldsymbol{r}_0^n = [x_0, y_0, z_0]^{\mathrm{T}}$ while the position of the mass is $\boldsymbol{r}^n = [x, y, z]^{\mathrm{T}} = \boldsymbol{r}_0^n + \boldsymbol{R}_b^n \boldsymbol{r}_r^b$, where $\boldsymbol{r}_r^b = [0, 0, L]^{\mathrm{T}}$. It follows that the velocity of the point mass is

$$\boldsymbol{v}^n = \boldsymbol{v}_0^n + \hat{\boldsymbol{\omega}}^n \boldsymbol{R}_b^n \boldsymbol{r}_r^b + \boldsymbol{R}_b^n \dot{\boldsymbol{r}}_r^b, \tag{2}$$

where $\hat{\boldsymbol{u}}$ is the skew symmetric form of a vector $\boldsymbol{u}$, $\boldsymbol{v}_0^n = [\dot{x}_0, \dot{y}_0, \dot{z}_0]^{\mathrm{T}}$ is the linear velocity of the suspension point, $\boldsymbol{\omega}^n = [\dot{\phi}_x, 0, 0]^{\mathrm{T}} + \boldsymbol{R}_x[0, \dot{\phi}_y, 0]^{\mathrm{T}}$ is the angular velocity of b relative to n. The components of the acceleration $\boldsymbol{a}^n = \dot{\boldsymbol{v}}^n = [\ddot{x}, \ddot{y}, \ddot{z}]^{\mathrm{T}}$ of the payload mass can then be found by time differentiation of the components in (2) to be

$$\ddot{x} = \ddot{x}_0 + Lc_y\ddot{\phi}_y - Ls_y\dot{\phi}_y^2 + 2\dot{L}c_y\dot{\phi}_y + \ddot{L}s_y, \tag{3}$$

$$\ddot{y} = \ddot{y}_0 + Ls_xc_y(\dot{\phi}_x^2 + \dot{\phi}_y^2) + 2Lc_xs_y\dot{\phi}_x\dot{\phi}_y - Lc_xc_y\ddot{\phi}_x + Ls_xs_y\ddot{\phi}_y + 2\dot{L}\left(-c_xc_y\dot{\phi}_x + s_xs_y\dot{\phi}_y\right) - \ddot{L}s_xc_y, \tag{4}$$

$$\ddot{z} = \ddot{z}_0 - Lc_xc_y(\dot{\phi}_x^2 + \dot{\phi}_y^2) + 2Ls_xs_y\dot{\phi}_x\dot{\phi}_y - Ls_xc_y\ddot{\phi}_x - Lc_xs_y\ddot{\phi}_y - 2\dot{L}\left(s_xc_y\dot{\phi}_x + c_xs_y\dot{\phi}_y\right) + \ddot{L}c_xc_y. \tag{5}$$

where $s_\alpha = \sin\phi_\alpha$ and $c_\alpha = \cos\phi_\alpha$.

2.2. Crane payload dynamics

The equations of motion for the payload can be derived with Kane's method (Kane & Levinson, 1985) with generalized speeds

$(\dot{\phi}_x, \dot{\phi}_y)$. The partial velocities are found from (2) to be

$$\boldsymbol{v}_1^n = \frac{\partial \boldsymbol{v}^n}{\partial \dot{\phi}_x} = \begin{bmatrix} 0 \\ -Lc_xc_y \\ -Ls_xc_y \end{bmatrix}, \quad \boldsymbol{v}_2^n = \frac{\partial \boldsymbol{v}^n}{\partial \dot{\phi}_y} = \begin{bmatrix} Lc_y \\ Ls_xs_y \\ -Lc_xs_y \end{bmatrix}. \tag{6}$$

Then the equations of motion are found from

$$(\boldsymbol{v}_i^n)^{\mathrm{T}}(-\boldsymbol{a}^n m + \boldsymbol{g}^n) = 0, \quad \text{for } i = 1, 2, \tag{7}$$

where $\boldsymbol{a}^n$ is given by (3)–(5), $\boldsymbol{g}^n = [0, 0, mg]^{\mathrm{T}}$ is the force of gravity where g =9.81 m s^{-2}. It follows that the equations of motion are

$$\ddot{\phi}_x c_y + \omega_0^2 s_x = \frac{\ddot{y}_0 c_x + \ddot{z}_0 s_x - 2\dot{L}c_y\dot{\phi}_x}{L} + 2s_y\dot{\phi}_x\dot{\phi}_y, \tag{8}$$

$$\ddot{\phi}_y + \omega_0^2 c_x s_y = \frac{-\ddot{x}_0 c_y - \ddot{y}_0 s_x s_y + \ddot{z}_0 c_x s_y - 2\dot{L}\dot{\phi}_y}{L} - s_y c_y \dot{\phi}_x^2, \tag{9}$$

where $\omega_0^2 = g/L$. An alternative derivation based on Lagrange's equation of motion is found in Abdel-Rahman et al. (2003). The acceleration of the suspension point $\boldsymbol{a}_0^n = [\ddot{x}_0, \ddot{y}_0, \ddot{z}_0]^{\mathrm{T}}$ and the hoisting rate $\dot{L}$ are considered to be control inputs. The cable length L is bounded by $0 < L_{\min} \leq L \leq L_{\max}$.

2.3. Crane dynamics

In this section the crane dynamics will be developed. The hoisting rate $\dot{L}$ is not considered in this section. The generalized coordinates of crane and payload are given by $\boldsymbol{q} = [\boldsymbol{q}_1^{\mathrm{T}}, \boldsymbol{q}_2^{\mathrm{T}}]^{\mathrm{T}}$ where $\boldsymbol{q}_1 = [\phi_x, \phi_y]^{\mathrm{T}}$ are the coordinates of the payload and

$$\boldsymbol{q}_2 = \begin{bmatrix} q_1 & q_2 & q_3 \end{bmatrix}^{\mathrm{T}} \in \mathbb{R}^3, \tag{10}$$

are the coordinates of the knuckle boom crane. The coordinates of the crane are shown in Fig. 1(b) with slewing joint q_1, and two prismatic actuators with stroke lengths q_2 and q_3. The input generalized forces corresponding to $\boldsymbol{q}_2$ are $\boldsymbol{\tau} = [\tau_1, \tau_2, \tau_3]^{\mathrm{T}}$. The dynamics of the crane and the payload are given by the underactuated system

$$\underbrace{\begin{bmatrix} \boldsymbol{M}_{11} & \boldsymbol{M}_{12} \\ \boldsymbol{M}_{21} & \boldsymbol{M}_{22} \end{bmatrix}}_{\boldsymbol{M}} \begin{bmatrix} \ddot{\boldsymbol{q}}_1 \\ \ddot{\boldsymbol{q}}_2 \end{bmatrix} + \begin{bmatrix} \boldsymbol{h}_1 \\ \boldsymbol{h}_2 \end{bmatrix} + \begin{bmatrix} \boldsymbol{\psi}_1 \\ \boldsymbol{\psi}_2 \end{bmatrix} = \begin{bmatrix} \boldsymbol{0} \\ \boldsymbol{\tau} \end{bmatrix} \tag{11}$$

where $\boldsymbol{h}_1 = \boldsymbol{C}_1(\boldsymbol{q}, \dot{\boldsymbol{q}})\dot{\boldsymbol{q}}$ and $\boldsymbol{h}_2 = \boldsymbol{C}_2(\boldsymbol{q}, \dot{\boldsymbol{q}})\dot{\boldsymbol{q}}$ are centrifugal and Coriolis terms, and $\boldsymbol{\psi}_1$ and $\boldsymbol{\psi}_2$ are gravitational terms. The mass matrix $\boldsymbol{M}$ is symmetric and positive definite. It follows that $\boldsymbol{M}_{11}$ and $\boldsymbol{M}_{22}$ are symmetric and positive definite, and that $\boldsymbol{M}_{12} = \boldsymbol{M}_{21}^{\mathrm{T}}$.

A change of variables is done by introducing $\boldsymbol{y} = \boldsymbol{h}(\boldsymbol{q}_2)$ where $\boldsymbol{y} = [x_0, y_0, z_0]^{\mathrm{T}}$ is the position of the tip of the crane. The velocity mapping is then $\dot{\boldsymbol{y}} = \boldsymbol{J}(\boldsymbol{q}_2)\dot{\boldsymbol{q}}_2$, and

$$\ddot{\boldsymbol{q}}_2 = \boldsymbol{J}^{-1}(\boldsymbol{q}_2)(\ddot{\boldsymbol{y}} - \dot{\boldsymbol{J}}(\boldsymbol{q}_2)\dot{\boldsymbol{q}}_2), \tag{12}$$

with Jacobian $\boldsymbol{J}(\boldsymbol{q}_2)$. In Tysse et al. (2021) the kinematics of the knuckle boom crane is described in details, including the Jacobian $\boldsymbol{J}(\boldsymbol{q}_2)$. The generalized force vector corresponding to the generalized coordinates $\boldsymbol{y}$ is $\boldsymbol{\sigma} = \boldsymbol{J}^{-\mathrm{T}}(\boldsymbol{q}_2)\boldsymbol{\tau}$. The dynamics can then be written

$$\boldsymbol{D}_{11}\ddot{\boldsymbol{q}}_1 + \boldsymbol{D}_{12}\ddot{\boldsymbol{y}} + \boldsymbol{c}_1 + \boldsymbol{\phi}_1 = \boldsymbol{0} \tag{13}$$

$$\boldsymbol{D}_{21}\ddot{\boldsymbol{q}}_1 + \boldsymbol{D}_{22}\ddot{\boldsymbol{y}} + \boldsymbol{c}_2 + \boldsymbol{\phi}_2 = \boldsymbol{\sigma} \tag{14}$$

where the mass matrix is

$$\boldsymbol{D} = \begin{bmatrix} \boldsymbol{D}_{11} & \boldsymbol{D}_{12} \\ \boldsymbol{D}_{21} & \boldsymbol{D}_{22} \end{bmatrix} = \begin{bmatrix} \boldsymbol{M}_{11} & \boldsymbol{M}_{12}\boldsymbol{J}^{-1} \\ \boldsymbol{J}^{-\mathrm{T}}\boldsymbol{M}_{21} & \boldsymbol{J}^{-\mathrm{T}}\boldsymbol{M}_{22}\boldsymbol{J}^{-1} \end{bmatrix}$$

and $\boldsymbol{c}_1 = \boldsymbol{h}_1 - \boldsymbol{D}_{12}\dot{\boldsymbol{J}}\dot{\boldsymbol{q}}_2$, $\boldsymbol{\phi}_1 = \boldsymbol{\psi}_1$, $\boldsymbol{c}_2 = \boldsymbol{J}^{-\mathrm{T}}(\boldsymbol{h}_2 - \boldsymbol{D}_{22}\dot{\boldsymbol{J}}\dot{\boldsymbol{q}}_2)$ and $\boldsymbol{\phi}_2 = \boldsymbol{J}^{-\mathrm{T}}\boldsymbol{\psi}_2$. It is straightforward to show that the mass matrix $\boldsymbol{D}$ is symmetric and positive definite whenever $\boldsymbol{M}$ is symmetric and positive definite. Moreover, $\boldsymbol{D}_{11}$ and $\boldsymbol{D}_{22}$ are positive definite.

3. Control strategy

The crane is assumed to be controlled by the generalized forces $\boldsymbol{\tau}$ from the actuators of the crane, while the Lyapunov controller and the NMPC controller are formulated with the acceleration of the crane tip as the control variables. To solve this problem, a control strategy is proposed based on partial feedback linearization as described in Spong (1994) and Shkolnik and Tedrake (2008). The actuated part of the system is the crane, while the crane payload is the unactuated part. In this setting, an exponentially stable Lyapunov-based controller is used to stabilize the crane payload dynamics to increase the damping of the pendulum oscillations. The stabilized dynamics is then controlled with a NMPC to control the motion of the crane tip with bounded pendulum motion for the payload.

3.1. Partial feedback linearization

The unactuated dynamics (13) can be written $\ddot{\boldsymbol{q}}_1 = -\boldsymbol{D}_{11}^{-1}(\boldsymbol{D}_{12}\ddot{\boldsymbol{y}} + \boldsymbol{c}_1 + \boldsymbol{\phi}_1)$ and substituted into the actuated dynamics (14), which gives

$$\bar{\boldsymbol{D}}_{22}\ddot{\boldsymbol{y}} + \bar{\boldsymbol{c}}_2 + \bar{\boldsymbol{\phi}}_2 = \boldsymbol{\sigma} \tag{15}$$

where $\bar{\boldsymbol{D}}_{22} = \boldsymbol{D}_{22} - \boldsymbol{D}_{21}\boldsymbol{D}_{11}^{-1}\boldsymbol{D}_{12}$ is symmetric and positive definite, $\bar{\boldsymbol{c}}_2 = \boldsymbol{c}_2 - \boldsymbol{D}_{21}\boldsymbol{D}_{11}^{-1}\boldsymbol{c}_1$ and $\bar{\boldsymbol{\phi}}_2 = \boldsymbol{\phi}_2 - \boldsymbol{D}_{21}\boldsymbol{D}_{11}^{-1}\boldsymbol{\phi}_1$. Partial feedback linearization is then achieved with the input generalized force vector

$$\boldsymbol{\sigma} = \bar{\boldsymbol{D}}_{22}\boldsymbol{v} + \bar{\boldsymbol{c}}_2 + \bar{\boldsymbol{\phi}}_2 \tag{16}$$

where $\boldsymbol{v}$ is a transformed control vector. The corresponding actuator forces are computed from $\boldsymbol{\tau} = \boldsymbol{J}(\boldsymbol{q}_2)^{\mathrm{T}}\boldsymbol{\sigma}$. The resulting partially linearized system is given by

$$\boldsymbol{D}_{11}\ddot{\boldsymbol{q}}_1 + \boldsymbol{c}_1 + \boldsymbol{\phi}_1 = -\boldsymbol{D}_{12}\boldsymbol{v} \tag{17}$$

$$\ddot{\boldsymbol{y}} = \boldsymbol{v} \tag{18}$$

It is seen that the acceleration $\ddot{\boldsymbol{y}} = \boldsymbol{v}$ appears as a control input to both the unactuated and the actuated part of the system.

Let the transformed control vector be

$$\boldsymbol{v} = \ddot{\boldsymbol{y}}^d - K_d\dot{\tilde{\boldsymbol{y}}} - K_p\tilde{\boldsymbol{y}} \tag{19}$$

where $\tilde{\boldsymbol{y}} = \boldsymbol{y} - \boldsymbol{y}^d$ and $K_p, K_d > 0$. This gives the cascaded closed loop dynamics

$$\boldsymbol{D}_{11}\ddot{\boldsymbol{q}}_1 + \boldsymbol{c}_1 + \boldsymbol{\phi}_1 = -\boldsymbol{D}_{12}(\ddot{\boldsymbol{y}}^d - K_d\dot{\tilde{\boldsymbol{y}}} - K_p\tilde{\boldsymbol{y}}) \tag{20}$$

$$\ddot{\tilde{\boldsymbol{y}}} + K_d\dot{\tilde{\boldsymbol{y}}} + K_p\tilde{\boldsymbol{y}} = 0 \tag{21}$$

where (20) is Lipschitz in the input $[\tilde{\boldsymbol{y}}^{\mathrm{T}}, \dot{\tilde{\boldsymbol{y}}}^{\mathrm{T}}]^{\mathrm{T}}$, and (21) is exponentially stable at $[\tilde{\boldsymbol{y}}^{\mathrm{T}}, \dot{\tilde{\boldsymbol{y}}}^{\mathrm{T}}]^{\mathrm{T}} = [\boldsymbol{0}^{\mathrm{T}}, \boldsymbol{0}^{\mathrm{T}}]^{\mathrm{T}}$.

It is noted that the closed loop dynamics (20) of the payload is a perturbation of

$$\boldsymbol{D}_{11}\ddot{\boldsymbol{q}}_1 + \boldsymbol{c}_1 + \boldsymbol{\phi}_1 = -\boldsymbol{D}_{12}\ddot{\boldsymbol{y}}^d \tag{22}$$

where the desired crane tip acceleration $\ddot{\boldsymbol{y}}^d = [\ddot{x}_0^d, \ddot{y}_0^d, \ddot{z}_0^d]^{\mathrm{T}}$ is the control variable. Note that the system (22) is equal to the system (17) except that the desired tip acceleration $\ddot{\boldsymbol{y}}^d$ has replaced the actual tip acceleration $\ddot{\boldsymbol{y}}$. The motion of the payload can therefore be controlled with the desired tip acceleration instead of the actual acceleration when the model (22) is used. Then, if $\ddot{\boldsymbol{y}}^d$ is selected so that (22) is exponentially stable, then the system (20)–(21) will be exponentially stable as will be explained in Section 5.2. This will be used in the controller design for the system.

3.2. Control of crane and crane payload

The desired acceleration $\ddot{\boldsymbol{y}}^d$ of the crane tip is the control input to the unactuated crane payload dynamics in (22) and at the same time the reference to the actuated crane dynamics, as seen from (19). This is solved by using

$$\ddot{\boldsymbol{y}}^d = \boldsymbol{u} + \boldsymbol{w} \tag{23}$$

where $\boldsymbol{u}$ is the control input from the Lyapunov-based controller for the crane payload, which is selected to make the unactuated dynamics (22) exponentially stable. The resulting closed loop dynamics of the crane payload is referred to as the stabilized crane payload dynamics. Then the control variable $\boldsymbol{w}$ is computed from the NMPC controller to control the crane motion and the stabilized crane payload dynamics. The NMPC is used to constraint the magnitude of the control input $\boldsymbol{w}$ so that the motion of the pendulum is bounded.

4. Lyapunov-based damping controller

4.1. Introduction

In this section a Lyapunov-based damping controller is presented. This controller is used to stabilize the dynamics of the pendulum, so that the pendulum will have better oscillation damping than in open loop. The Lyapunov-based damping controller is designed so that it can be combined with a tracking controller for the crane tip. The controller design for the tracking controller will then be less demanding due to the improved dynamics of the pendulum. In particular, if the tracking controller is controlled with a NMPC, then the NMPC can have lower sampling frequency and less complexity compared to a solution where no damping controller is used and the NMPC must also handle oscillation damping. Moreover the damping controller can be used for initial damping of the payload oscillations before the tracking controller is switched on.

4.2. Energy-based oscillation damping for stationary crane

In this section, an energy-based damping controller is designed to stabilize the system (8)–(9) about the equilibrium point when the position $\boldsymbol{r}_0^n$ of the suspension point is nominally stationary, and the pendulum length L is fixed. This controller is extended in the next section to oscillation damping in combination with motion tracking for the payload. The damping controller is derived using the desired horizontal acceleration $(\ddot{x}_0^d, \ddot{y}_0^d)$ of the suspension point as control input. It is assumed that $\ddot{z}_0^d = 0$ and $\dot{L}^d = 0$. The damping controller is given by the feedback control laws

$$\ddot{x}_0^d = 2\zeta\omega_0 L\dot{\phi}_y - \ddot{y}_0^d s_x s_y/c_y, \quad \ddot{y}_0^d = -2\zeta\omega_0 L\dot{\phi}_x, \tag{24}$$

where ζ is a positive parameter to be chosen. Insertion of the feedback control laws (24) into the equations of motion (8)–(9) gives the closed-loop dynamics

$$\ddot{\phi}_x c_y + 2\zeta\omega_0\dot{\phi}_x c_x + \omega_0^2 s_x = 2\dot{\phi}_x\dot{\phi}_y s_y, \tag{25}$$

$$\ddot{\phi}_y + 2\zeta\omega_0\dot{\phi}_y c_y + \omega_0^2 c_x s_y = -\dot{\phi}_x^2 s_y c_y. \tag{26}$$

where the desired accelerations have replaced the actual accelerations in the equations of motion (8)–(9) as in (22). Linearization of (25)–(26) about the equilibrium $\phi_x = \phi_y = 0$ and $\dot{\phi}_x = \dot{\phi}_y = 0$ yields

$$\ddot{\phi}_i + 2\zeta\omega_0\dot{\phi}_i + \omega_0^2\phi_i = 0, \quad \text{for } i = x, y. \tag{27}$$

It is seen that the linearized closed-loop model is represented by two harmonic oscillators with relative damping ζ and undamped natural frequency ω_0. The stability of the nonlinear closed-loop model (25)–(26) can be analyzed with the energy function

$$V_d = 0.5mL^2\left(\dot{\phi}_x^2 c_y^2 + \dot{\phi}_y^2\right) + mgL(1 - c_x c_y), \tag{28}$$

which is the kinetic energy and potential energy of the pendulum with a stationary suspension point. Time differentiation of V_d along the trajectories of the solutions of (8)–(9) gives

$$\dot{V}_d = mL\dot{\phi}_x c_y\ddot{y}_0 c_x - mL\dot{\phi}_y\left(\ddot{x}_0 c_y + \ddot{y}_0 s_x s_y\right). \tag{29}$$

Substitution of the feedback control laws (24) gives the time derivative of the energy function V_d along the trajectories of the solutions of (25)–(26)

$$\dot{V}_d = -2\zeta\omega_0 mL^2\left(\dot{\phi}_x^2 c_x c_y + \dot{\phi}_y^2 c_y\right). \tag{30}$$

From LaSalle's theorem (Khalil, 2002) we can conclude that the equilibrium $\phi_x = \phi_y = 0$ and $\dot{\phi}_x = \dot{\phi}_y = 0$ of the closed-loop dynamics (25)–(26) is asymptotically stable.

4.3. Oscillation damping for moving crane

The next step is to design an exponentially stable damping controller for the spherical pendulum system (8)–(9). The control laws are $\ddot{x}_0^d = u_x$ and $\ddot{y}_0^d = u_y$ where

$$u_x = \frac{L}{c_y}(k_d\dot{\phi}_y + k_p\phi_y) - Ls_y\dot{\phi}_x^2 - \frac{u_y s_x s_y}{c_y}, \tag{31}$$

$$u_y = -\frac{Lc_y}{c_x}(k_d\dot{\phi}_x + k_p\phi_x) - \frac{2Ls_y}{c_x}\dot{\phi}_x\dot{\phi}_y + g\frac{s_x {s_y}^2}{c_x}. \tag{32}$$

The feedback control law is seen to be a PD controller with gains k_p and k_d with some higher-order cancellation terms, which will be small. Insertion of the control laws (31)–(32) into the equations of motion (8)–(9) using $c_y s_x = s_x/c_y - s_x s_y^2/c_y$ gives the closed loop dynamics

$$\ddot{\phi}_x + k_d\dot{\phi}_x + k_p\phi_x + \omega_0^2 c_y s_x = 0, \tag{33}$$

$$\ddot{\phi}_y + k_d\dot{\phi}_y + k_p\phi_y + \omega_0^2 c_x s_y = 0. \tag{34}$$

This is referred to as the stabilized pendulum dynamics. It is noted that linearization of the stabilized dynamics gives two harmonic oscillators with undamped natural frequency $\omega_n^2 = k_p + \omega_0^2$ and relative damping $\zeta = k_d/2\omega_n$. This can be used to find controller gains k_p and k_d.

4.4. Lyapunov Function

Consider the state vector $\boldsymbol{x} = [\phi_x, \dot{\phi}_x, \phi_y, \dot{\phi}_y]^{\mathrm{T}}$ and the domain

$$D = \left\{\boldsymbol{x} \;\middle|\; |\phi_j| < \frac{\pi}{2} - \delta \text{ and } \left|\dot{\phi}_j\right| \le \zeta\right\} \text{ for } j = x, y, \tag{35}$$

where $0 < \zeta < \pi$ and $0 < \delta < \pi/2$. The Lyapunov function candidate

$$V(\boldsymbol{x}) = 0.5L^2\boldsymbol{x}^{\mathrm{T}}\boldsymbol{P}\boldsymbol{x} + mgL\left(1 - c_x c_y\right), \tag{36}$$

is used, where

$$\boldsymbol{P} = \begin{bmatrix}\boldsymbol{P}_1 & \boldsymbol{0}\\ \boldsymbol{0} & \boldsymbol{P}_1\end{bmatrix}, \quad \boldsymbol{P}_1 = \begin{bmatrix}p_{11} & p_{12}\\ p_{12} & p_{22}\end{bmatrix}. \tag{37}$$

is symmetric and positive definite with elements given by

$$p_{11} = (k_p + ck_d)p_{22}, \quad p_{12} = cp_{22}, \quad p_{22} = m, \tag{38}$$

where $0 < c < k_d$. It is seen from (38) that

$$p_{11} - p_{12}k_d - p_{22}k_p = 0. \tag{39}$$

As proposed in Wen and Bayard (1988), the introduction of a nonzero off-diagonal term p_{12} in the matrix $\boldsymbol{P}$ gives a cross term

in the Lyapunov function candidate which is needed to establish exponential stability. Given that $p_{11} > 0$ and

$$\begin{vmatrix} p_{11} & p_{12} \\ p_{12} & p_{22} \end{vmatrix} = \left((k_p + ck_d) - c^2\right) p_{22}^2 > 0, \tag{40}$$

it can be concluded that $\boldsymbol{P}$ is a real symmetric positive definite matrix with positive eigenvalues (Golub & Van Loan, 1996). Since $|\sin\alpha| \leq |\alpha|$ it follows that $\sin^2(\alpha/2) \leq \alpha^2/4$. Together with $\cos\alpha = 1 - 2\sin^2(\alpha/2)$, this gives $\cos\alpha \geq 1 - \alpha^2/2$. From this it is clear that $0 \leq \left(1 - c_x c_y\right) \leq 0.5\left(\phi_x^2 + \phi_y^2\right)$ in D. Using this condition, it is seen from (36) that

$$0.5L_{\min}^2 \boldsymbol{x}^{\mathrm{T}}\boldsymbol{P}\boldsymbol{x} \leq V(\boldsymbol{x}) \leq 0.5L_{\max}^2 \boldsymbol{x}^{\mathrm{T}}\tilde{\boldsymbol{P}}\boldsymbol{x}, \quad \forall \boldsymbol{x} \in D \tag{41}$$

where $\tilde{\boldsymbol{P}} = \boldsymbol{P} + mg\,\mathrm{diag}(1, 0, 1, 0)/L_{\max}$, and $L_{\min}$ and $L_{\max}$ denotes the lower and upper bound on the cable length, respectively. Consequently, from the results in (41), the Lyapunov function candidate can be upper and lower bounded by

$$k_1\|\boldsymbol{x}\|_2^2 \leq V(\boldsymbol{x}) \leq k_2\|\boldsymbol{x}\|_2^2, \quad \forall \boldsymbol{x} \in D, \tag{42}$$

where $k_1 = 0.5L_{\min}^2\lambda_{\min}(\boldsymbol{P})$ and $k_2 = 0.5L_{\max}^2\lambda_{\max}(\tilde{\boldsymbol{P}})$ are positive constants, and $\lambda_{\min}(\boldsymbol{P})$ is the smallest eigenvalue of $\boldsymbol{P}$ and $\lambda_{\max}(\tilde{\boldsymbol{P}})$ is the largest eigenvalue of $\tilde{\boldsymbol{P}}$.

It is concluded that the Lyapunov function $V(\boldsymbol{x})$ in (42) is positive definite and decrescent in the domain D.

4.5. Exponential stability

The time derivative of $V(\boldsymbol{x})$ along the trajectories of the solutions of (33)–(34), denoted by $\dot{V}(\boldsymbol{x})$, is given by

$$\begin{aligned}\dot{V}(\boldsymbol{x}) = {} & L^2\left(\dot{\phi}_x\phi_x + \dot{\phi}_y\phi_y\right)(p_{11} - p_{12}k_d - p_{22}k_p) \\ & - L^2 p_{12}k_p(\phi_x^2 + \phi_y^2) - L^2 p_{22}k_d(\dot{\phi}_x^2 + \dot{\phi}_y^2) \\ & - L^2 p_{12}\omega_0^2\left(\phi_x s_x c_y + \phi_y s_y c_x\right) + L^2 p_{12}\left(\dot{\phi}_x^2 + \dot{\phi}_y^2\right) \\ & + \left(\dot{\phi}_x s_x c_y + \dot{\phi}_y c_x s_y\right)\left(mgL - L^2 p_{22}\omega_0^2\right) \\ & + \dot{L}L\boldsymbol{x}^{\mathrm{T}}\boldsymbol{P}\boldsymbol{x} + \dot{L}mg(1 - c_x c_y).\end{aligned} \tag{43}$$

Insertion of (38), (39) and $\omega_0^2 = g/L$ into (43) gives

$$\begin{aligned}\dot{V}(\boldsymbol{x}) = {} & -L^2 p_{12}k_p(\phi_x^2 + \phi_y^2) - L^2\left(p_{22}k_d - p_{12}\right)\left(\dot{\phi}_x^2 + \dot{\phi}_y^2\right) \\ & - L^2 p_{12}\omega_0^2\left(\phi_x s_x c_y + \phi_y s_y c_x\right) \\ & + \dot{L}L\boldsymbol{x}^{\mathrm{T}}\boldsymbol{P}\boldsymbol{x} + \dot{L}mg(1 - c_x c_y).\end{aligned} \tag{44}$$

Since $\alpha\sin\alpha \geq 0$ and $\cos\alpha \geq 0$ when $|\alpha| < \pi/2$, it follows that $\phi_x s_x c_y + \phi_y c_x s_y \geq 0$ and $p_{22}k_d - p_{12} > 0$ in D. Then, if the hoisting rate is bounded by $|\dot{L}| \leq \gamma_L$, it follows from (42)–(43) that $\dot{L}L\boldsymbol{x}^{\mathrm{T}}\boldsymbol{P}\boldsymbol{x} + \dot{L}mg(1 - c_x c_y) \leq 2\gamma_L k_2\|\boldsymbol{x}\|_2^2/L$. Using these conditions and $L_{\min} \leq L$, it follows that

$$\begin{aligned}\dot{V}(\boldsymbol{x}) \leq {} & -L_{\min}^2\left[p_{12}k_p(\phi_x^2 + \phi_y^2) + \left(p_{22}k_d - p_{12}\right)\left(\dot{\phi}_x^2 + \dot{\phi}_y^2\right)\right] \\ & + 2\gamma_L k_2\|\boldsymbol{x}\|_2^2/L_{\min},\end{aligned} \tag{45}$$

which leads to

$$\dot{V}(\boldsymbol{x}) \leq -k_3\|\boldsymbol{x}\|_2^2, \quad \forall \boldsymbol{x} \in D, \tag{46}$$

where $k_3 = L_{\min}^2\min\{p_{12}k_p, p_{22}k_d - p_{12}\} - 2\gamma_L k_2/L_{\min}$ and

$$0 \leq \gamma_L < L_{\min}^3\min\{p_{12}k_p, p_{22}k_d - p_{12}\}/(2k_2). \tag{47}$$

It follows that the equilibrium point of the closed-loop dynamics (33)–(34) is exponentially stable in D when $0 < c < k_d$ and $0 < k_p$.

4.6. Nonvanishing perturbations

In this section the effect of nonvanishing perturbations for the exponentially stable system will be analyzed following the presentation in Khalil (2002). The motivation for this is that a bounded nonvanishing perturbation of the exponentially stable system will give a system with bounded perturbations.

The desired tip accelerations and the desired hoisting rate are written

$$\ddot{x}_0^d = u_x + g_x, \quad \ddot{y}_0^d = u_y + g_y, \tag{48}$$

$$\ddot{z}_0^d = g_z, \quad \dot{L}^d = g_L \tag{49}$$

where u_x and u_y are given by the Lyapunov controller (31)–(32) and the terms g_x, g_y, g_z, g_L are referred to as nonvanishing perturbations.

Insertion of the control variables in (48)–(49) into the equations of motion (8)–(9) gives the closed-loop dynamics

$$\ddot{\phi}_x + k_d\dot{\phi}_x + k_p\phi_x + \omega_0^2 c_y s_x - \frac{1}{c_y L}(g_y c_x + g_z s_x - 2g_L\dot{\phi}_x c_y) = 0, \tag{50}$$

$$\begin{aligned}&\ddot{\phi}_y + k_d\dot{\phi}_y + k_p\phi_y + \omega_0^2 c_x s_y \\ &\quad + (g_x c_y + g_y s_x s_y - g_z c_x s_y + 2g_L\dot{\phi}_y)/L = 0.\end{aligned} \tag{51}$$

This is referred to as the perturbed stabilized pendulum dynamics. The time derivative of $V(\boldsymbol{x})$ along the trajectories of the perturbed system (50)–(51) will then satisfy

$$\begin{aligned}\dot{V}(\boldsymbol{x}) \leq {} & -k_3\|\boldsymbol{x}\|_2^2 + \frac{L}{c_y}(p_{12}\phi_x + p_{22}\dot{\phi}_x)(g_y c_x + g_z s_x - 2g_L\dot{\phi}_x c_y) \\ & - L(p_{12}\phi_y + p_{22}\dot{\phi}_y)(g_x c_y + g_y s_x s_y - g_z c_x s_y + 2g_L\dot{\phi}_y), \\ \leq {} & -k_3\|\boldsymbol{x}\|_2^2 + \alpha_x g_x + \alpha_y g_y + \alpha_z g_z + \alpha_L g_L,\end{aligned} \tag{52}$$

where

$$\alpha_x = -Lc_y(p_{12}\phi_y + p_{22}\dot{\phi}_y),$$

$$\alpha_y = -Ls_x s_y(p_{12}\phi_y + p_{22}\dot{\phi}_y) + \frac{Lc_x}{c_y}(p_{12}\phi_x + p_{22}\dot{\phi}_x),$$

$$\alpha_z = Lc_x s_y(p_{12}\phi_y + p_{22}\dot{\phi}_y) + \frac{Ls_x}{c_y}(p_{12}\phi_x + p_{22}\dot{\phi}_x),$$

$$\alpha_L = -2L\left((p_{12}\phi_y + p_{22}\dot{\phi}_y)\dot{\phi}_y + (p_{12}\phi_x + p_{22}\dot{\phi}_x)\dot{\phi}_x\right).$$

It is assumed that the perturbations (g_x, g_y, g_z, g_L) are uniformly bounded according to $|g_x(t)| \leq \gamma$, $|g_y(t)| \leq \gamma$, $|g_z(t)| \leq \gamma$, $|g_L(t)| \leq \gamma_L$, $0 \leq \gamma_L < L_{\min}^3\min\{p_{12}k_p, p_{22}k_d - p_{12}\}/(2k_2)$ and $\gamma_L \leq \gamma/\zeta$ $\forall t \geq 0$ where the property in (47) has been used and ζ is defined in (35). The time derivative of $V(\boldsymbol{x})$ along the trajectories of the solutions of (50)–(51) can then be expressed as

$$\dot{V}(\boldsymbol{x}) \leq -k_3\|\boldsymbol{x}\|_2^2 + \gamma\alpha, \tag{53}$$

where $\alpha = \alpha_x + \alpha_y + \alpha_z + \alpha_L/\zeta$. The scalars α_x, α_y, α_z and α_L satisfy

$$\alpha_x \leq L_{\max}(p_{12}|\phi_y| + p_{22}|\dot{\phi}_y|),$$

$$\alpha_y \leq L_{\max}(p_{12}|\phi_y| + p_{22}|\dot{\phi}_y|) + \frac{L_{\max}(p_{12}|\phi_x| + p_{22}|\dot{\phi}_x|)}{c_1},$$

$$\alpha_z \leq L_{\max}(p_{12}|\phi_y| + p_{22}|\dot{\phi}_y|) + \frac{L_{\max}(p_{12}|\phi_x| + p_{22}|\dot{\phi}_x|)}{c_1},$$

$$\alpha_L \leq 2\zeta L_{\max}\left(p_{12}|\phi_x| + p_{22}|\dot{\phi}_x| + p_{12}|\phi_y| + p_{22}|\dot{\phi}_y|\right),$$

where it is used that $c_1 = \cos(\pi/2 - \delta) \leq c_y$, $|c_x| \leq 1$, $|c_y| \leq 1$, $|s_x| \leq 1$, $|s_x s_y| \leq 1$, $|c_x s_y| \leq 1$, $L \leq L_{\max}$ and $|\dot{\phi}_j| \leq \zeta$ for $j = x, y$. These properties are valid for all $\boldsymbol{x} \in D$. It is clear that

$$\alpha \leq \frac{2L_{\max}(c_1 + 1)(p_{12}|\phi_x| + p_{22}|\dot{\phi}_x|)}{c_1} + 5L_{\max}(p_{12}|\phi_y| + p_{22}|\dot{\phi}_y|),$$

$$\leq k_4\|\boldsymbol{x}\|_2, \tag{54}$$

where $k_4 = \frac{L_{\max}}{c_1}\sqrt{(4(c_1+1)^2+25c_1^2)(p_{12}^2+p_{22}^2)}$. Given that $0 < \theta < 1$, the time derivative of $V(\boldsymbol{x})$ along the trajectories of the solutions of (50)–(51) satisfies

$$\begin{aligned}\dot{V}(\boldsymbol{x}) &\leq -k_3\|\boldsymbol{x}\|_2^2 + k_4\gamma\|\boldsymbol{x}\|_2,\\ &\leq -(1-\theta)\,k_3\|\boldsymbol{x}\|_2^2, \quad \forall\,\|\boldsymbol{x}\|_2 \geq \gamma k_4/\theta k_3.\end{aligned} \tag{55}$$

This shows that $\boldsymbol{x}$ will be ultimately bounded in the presence of nonvanishing perturbations. The solution of the perturbed system (50)–(51) satisfies

$$\|\boldsymbol{x}(t)\|_2 \leq ke^{-\varphi t}\|\boldsymbol{x}(0)\|_2, \quad \forall\, t < T, \tag{56}$$

and

$$\|\boldsymbol{x}(t)\|_2 \leq b, \quad \forall\, t \geq T, \tag{57}$$

for some finite T, where $k = \sqrt{k_2/k_1}$, $\varphi = (1-\theta)k_3/(2k_2)$ and $b = k_4\gamma k/(k_3\theta)$.

5. Nonlinear MPC

5.1. Nonlinear MPC controller

In this section an NMPC is designed for the perturbed stabilized pendulum dynamics (50)–(51). The goal of the controller is to make the crane tip can follow a desired position trajectory. This is done by using the perturbation vector

$$\boldsymbol{v} = \begin{bmatrix}\boldsymbol{w}^{\mathrm{T}} & g_L\end{bmatrix}^{\mathrm{T}}, \quad \boldsymbol{w} = \begin{bmatrix}g_x & g_y & g_z\end{bmatrix}^{\mathrm{T}} \tag{58}$$

as control variables in the NMPC controller to control the position (x_0, y_0, z_0) of the suspension point, and the cable length L.

The system dynamics to be controlled by the NMPC is given by the perturbed stabilized pendulum dynamics (50)–(51), where the pendulum dynamics are stabilized by the Lyapunov controller (31)–(32). The resulting dynamics of the system controlled by the NMPC are

$$\ddot{x}_0 = g_x + \frac{L(k_d\dot{\phi}_y + k_p\phi_y) - Lc_ys_y\dot{\phi}_x^2 - u_ys_xs_y}{c_y}, \tag{59}$$

$$\ddot{y}_0 = g_y - \frac{Lc_y(k_d\dot{\phi}_x + k_p\phi_x) + 2Ls_y\dot{\phi}_x\dot{\phi}_y - gs_xs_y^2}{c_x}, \tag{60}$$

$$\ddot{z}_0 = g_z, \quad \dot{L} = g_L, \tag{61}$$

$$\ddot{\phi}_x = -k_d\dot{\phi}_x - k_p\phi_x - \omega_0^2c_ys_x + \frac{1}{c_yL}(g_yc_x + g_zs_x - 2g_L\dot{\phi}_xc_y), \tag{62}$$

$$\begin{aligned}\ddot{\phi}_y = &-k_d\dot{\phi}_y - k_p\phi_y - \omega_0^2c_xs_y\\ &-(g_xc_y + g_ys_xs_y - g_zc_xs_y + 2g_L\dot{\phi}_y)/L.\end{aligned} \tag{63}$$

The state vector is defined as

$$\boldsymbol{z} = [x_0\ \dot{x}_0\ y_0\ \dot{y}_0\ z_0\ \dot{z}_0\ L\ \phi_x\ \dot{\phi}_x\ \phi_y\ \dot{\phi}_y]^{\mathrm{T}}. \tag{64}$$

and the control vector is given by (58). The NMPC problem can then be written

$$\dot{\boldsymbol{z}}(t) = \boldsymbol{f}(\boldsymbol{z}(t), \boldsymbol{v}(t)), \quad \boldsymbol{z}(0) = \boldsymbol{z}_0, \tag{65}$$

$$\boldsymbol{v}(t) \in \mathbb{U},\ \forall t \geq 0 \text{ and } \boldsymbol{z}(t) \in \mathbb{X},\ \forall t \geq 0, \tag{66}$$

$$\mathbb{U} = \left\{\boldsymbol{v} \mid |g_x| < \gamma, |g_y| < \gamma, |g_z| < \gamma, |g_L| < \gamma_L\right\}, \tag{67}$$

$$\mathbb{X} = \{\boldsymbol{z} \mid L_{\min} \leq L \leq L_{\max}\}. \tag{68}$$

where $\boldsymbol{f}$ is given by (59)–(63). The NMPC samples the state $\boldsymbol{z}_k = \boldsymbol{z}(t_k)$ at a time t_k, then it predicts the future response of the system (65). The optimal control vector $\boldsymbol{v}_k$ is determined by minimizing an open-loop objective function over a prediction horizon T_p (Findeisen & Allgöwer, 2002; Grüne & Pannek, 2013). This process is repeated at the next sample of t_{k+1}, and a new control vector $\boldsymbol{v}_{k+1}$ is calculated. We denote the internal state and control vector in the NMPC by a bar (for example $\bar{\boldsymbol{z}}$, $\bar{\boldsymbol{v}}$), to distinguish them from the variables in the real system in (65). The system in (65) is described in continuous-time, while the required formulation for the NMPC controller is discrete-time (Mayne et al., 2000). The discrete-time model of (65) driven by the input $\boldsymbol{v}$, is

$$\bar{\boldsymbol{z}}_{k+1} = \boldsymbol{f}_k(\bar{\boldsymbol{z}}_k, \bar{\boldsymbol{v}}_k),\ \bar{\boldsymbol{z}}_0 = \boldsymbol{z}(t),\ k = 0, \ldots, M-1, \tag{69}$$

where $M = T_p/h$ is the number of prediction steps, h is the time step and T_p is the prediction horizon. The discrete-time model was obtained by using a repeated application of Euler's method as described in Mills et al. (2009) and Tysse and Egeland (2019). The control problem described above is mathematically formulated as follows:

$$\min_{\bar{\boldsymbol{v}}_k}\left(\sum_{k=0}^{M-1}\|\bar{\boldsymbol{z}}_k - \bar{\boldsymbol{z}}_r\|_{\boldsymbol{Q}}^2 + \sum_{k=1}^{M-1}\|\bar{\boldsymbol{v}}_k - \bar{\boldsymbol{v}}_{k-1}\|_{\boldsymbol{R}}^2\right), \tag{70}$$

subject to $\bar{\boldsymbol{z}}_0 = \boldsymbol{z}(t)$, $\bar{\boldsymbol{z}}_{k+1} = \boldsymbol{f}_k(\bar{\boldsymbol{z}}_k, \bar{\boldsymbol{v}}_k)$, $\bar{\boldsymbol{z}}_r = \boldsymbol{z}_r(t)$, $\bar{\boldsymbol{v}}_k \in \mathbb{U}$ and $\bar{\boldsymbol{z}}_k \in \mathbb{X}$ for $k = 0, \ldots, M-1$. Here, $\boldsymbol{z}_r = [x_r\ \dot{x}_r\ y_r\ \dot{y}_r\ z_r\ \dot{z}_r\ L_r\ 0\ 0\ 0\ 0]^{\mathrm{T}}$ is the time-varying state reference. The weight matrices are

$$\boldsymbol{Q} = \mathrm{diag}(Q_x, Q_{\dot{x}}, Q_y, Q_{\dot{y}}, Q_z, Q_{\dot{z}}, Q_L, 0, 0, 0, 0), \tag{71}$$

$$\boldsymbol{R} = \mathrm{diag}(R_x, R_y, R_z, R_L). \tag{72}$$

The weight matrix $\boldsymbol{Q}$ penalizes the deviations of the actual cable length, suspension point position and velocity from the desired cable length, suspension point position and velocity. The weight matrix $\boldsymbol{R}$ penalizes changes in the future manipulated control inputs $\boldsymbol{v}$. The internal states $\{\bar{\boldsymbol{z}}_1, \ldots, \bar{\boldsymbol{z}}_M\}$ are the results of (69) steered by the control inputs $\bar{\boldsymbol{v}}(\cdot; \boldsymbol{z}(t)) = \{\bar{\boldsymbol{v}}_0, \ldots, \bar{\boldsymbol{v}}_{M-1}\} : [t, t+T_p] \to \mathbb{U}$ with the initial state $\boldsymbol{z}(t)$. The closed-loop control $\boldsymbol{v}$ is defined by the optimal control vector $\bar{\boldsymbol{v}}^*(\cdot; \boldsymbol{z}(t))$ that minimizes the cost function $J(\boldsymbol{z}(t), \bar{\boldsymbol{v}}(\cdot))$ in (70). The optimal control vector is recalculated at each sampling instant τ. In the simulation study, the NMPC was implemented with the MATLAB function `fmincon` with an SQP algorithm, while in the experiment the NMPC was implemented in C++ using CasADi (Andersson et al., 2019). The optimization problem was solved by the NLP solver IPOPT, which is an interior point method interfaced with CasADi (Wächter & Biegler, 2006). A block diagram of the controller presented is given in Fig. 2.

5.2. Overall stability analysis

The overall stability of the system is analyzed in this section. The system is controlled with partial feedback linearization with input generalized forces given by (16), where the transformed control vector $\boldsymbol{v}$ is given by (19). The resulting dynamic model of crane and the crane payload is given by (20) and (21). It is noted that the dynamics (20) of the unactuated part is a perturbation of (22).

The desired acceleration of the crane tip is set to $\ddot{\boldsymbol{y}}^d = \boldsymbol{u} + \boldsymbol{w}$ where $\boldsymbol{u} = [u_x, u_y, 0]^{\mathrm{T}}$ where u_x and u_y is the control input from the Lyapunov-based controller, which is given by (31) and (32). The control input from the NMPC is $\boldsymbol{v} = [\boldsymbol{w}^{\mathrm{T}}, g_L]^{\mathrm{T}}$ where $\boldsymbol{w}$ controls the crane tip and g_L controls the hoisting rate. Consider first the case where $\boldsymbol{w} = \boldsymbol{0}$. Then (22) with $\ddot{\boldsymbol{y}}^d = \boldsymbol{u}$ is exponentially stable at $[\boldsymbol{q}_1^{\mathrm{T}}, \dot{\boldsymbol{q}}_1^{\mathrm{T}}]^{\mathrm{T}} = [\boldsymbol{0}^{\mathrm{T}}, \boldsymbol{0}^{\mathrm{T}}]^{\mathrm{T}}$ as shown in Section 4.5. Since (20) is a perturbation of (22) which is Lipschitz in the inputs $\tilde{\boldsymbol{y}}$ and $\dot{\tilde{\boldsymbol{y}}}$, it follows that (20) will be input-to-state stable (Khalil, 2002, p. 176), and the cascaded system (20)–(21) will be exponentially stable (Khalil, 2002, p. 537).

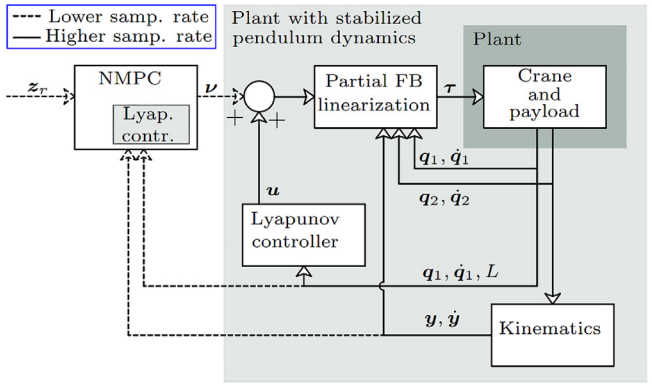

Fig. 2. Block diagram of the control system. The Lyapunov controller stabilizes the system dynamics at a high sampling frequency, and the NMPC controls the stabilized system at a slower sampling frequency. The stabilization of the system with the Lyapunov controller reduces the complexity of the NMPC design and implementation.

Consider then the case $\ddot{\boldsymbol{y}}^d = \boldsymbol{u}+\boldsymbol{w}$ where $\boldsymbol{v} = [\boldsymbol{w}^{\mathrm{T}}, g_L]^{\mathrm{T}} \in \mathbb{U}$ and $\mathbb{U}$ is defined in (68). Then the control input $\boldsymbol{w}$ will be a uniformly bounded nonvanishing perturbation to the exponentially stable system (20)–(21) and the control input $\boldsymbol{v}$ will be a uniformly bounded nonvanishing perturbation to the exponentially stable pendulum system (33)–(34). It follows that the reference $\boldsymbol{z}_r$ to the NMPC will be tracked with uniformly bounded deviations in $\boldsymbol{q}_1$ and $\dot{\boldsymbol{q}}_1$.

5.3. Implementation issues

The actuators of an industrial knuckle boom crane will be controlled by velocity controllers, so it may not be possible to implement partial feedback linearization. An approximate solution is to use the velocity loops as in Rauscher et al. (2018). Then the commanded accelerations are integrated to commanded velocities. The velocity loops are given by

$$\dot{w}_x = u_x + g_x, \quad \dot{w}_y = u_y + g_y, \quad \dot{w}_z = g_z, \tag{73}$$

$$\ddot{x}_0 = \frac{1}{T_v}(w_x - \dot{x}_0), \quad \ddot{y}_0 = \frac{1}{T_v}(w_z - \dot{y}_0), \tag{74}$$

$$\ddot{z}_0 = \frac{1}{T_v}(w_z - \dot{z}_0). \tag{75}$$

The bandwidth $1/T_v$ of the velocity loop must be significantly faster than the bandwidth of the combined NMPC and Lyapunov-based damping controller. This solution worked well in simulations and experiments on a laboratory crane.

6. Simulation and experiments

6.1. Simulation study

The performance of the proposed control system was investigated in a simulation study. The desired reference path (x_r, y_r, z_r, L_r) used in the simulation study is shown in Fig. 3(a). In the figure it is shown that the reference path of the suspension point was close to a circular helix segment with a 90° rotation about the z axis of the crane base, a radius of approximately 2 m and a pitch of approximately −2.4 m/rad. The reference path is initialized at (x_i, y_i, z_i, L_1), then the payload is hoisted to (x_i, y_i, z_i, L_2), then it follows a circular helix motion to (x_f, y_f, z_f, L_2), and at final the payload is lowered to (x_f, y_f, z_f, L_1). The path parameters $x_i, \ldots, L_2$ are given in Table 2.

In Fig. 3(b) the reference input $\boldsymbol{z}_r$ is shown. The trajectory for the suspension point is a piece-wise linear approximation

Table 1
Control parameters used in simulation and experiments. Q_i denotes the elements of the state weight matrix $\boldsymbol{Q}$.

Term	Value	Term	Value	Term	Value
T_v	0.1 s	k_p	1	M	4
h	0.2 s	k_d	2	Q_i	1
τ	0.4 s				

Table 2
Parameters used in simulation and experiments.

Term	Simulation	Experiments
(x_i, y_i, z_i)	(1.7, 1.02, −0.4) m	(1.7, 1.02, −1.0) m
(x_f, y_f, z_f)	(−1.02, 1.7, −1.0) m	(0.5, 1.9, −1.0) m
$(\lvert\gamma_1\rvert, \lvert\gamma\rvert)$	$(0.2\,\mathrm{m\,s^{-1}},\ 0.2\,\mathrm{m\,s^{-2}})$	$(0\,\mathrm{m\,s^{-1}},\ 0.1\,\mathrm{m\,s^{-2}})$
(L_1, L_2)	(1.7, 1.05) m	(1.05, 1.05) m
$(L_{\min}, L_{\max})$	(1.05, 1.7) m	(1.05, 1.05) m
$(\phi_x(0), \phi_y(0))$	$(10°, -10°)$	

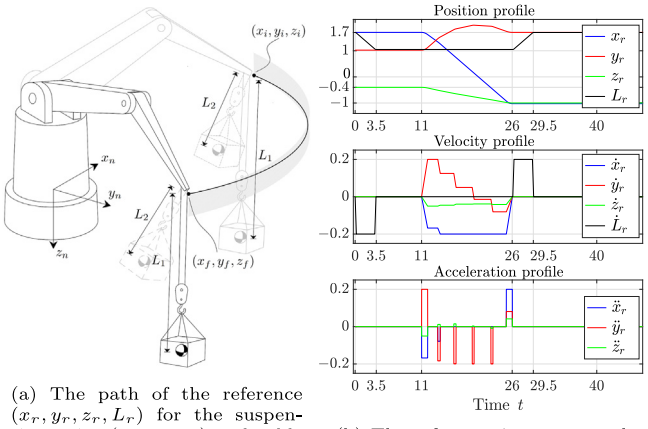

(a) The path of the reference (x_r, y_r, z_r, L_r) for the suspension point (x_0, y_0, z_0) and cable length L, where $\boldsymbol{p}_i = (x_i, y_i, z_i)$ and $\boldsymbol{p}_f = (x_f, y_f, z_f)$ denotes the initial and final reference point for the suspension point, respectively.

(b) The reference input $\boldsymbol{z}_r$ used in the simulation study. Position (x_r, y_r, z_r, L_r) given in m, velocity $(\dot{x}_r, \dot{y}_r, \dot{z}_r, \dot{L}_r)$ given in m/s and acceleration $(\ddot{x}_r, \ddot{y}_r, \ddot{z}_r)$ profiles given in $\mathrm{m/s^2}$ are shown.

Fig. 3. Path and trajectory for the reference input.

of the helix segment and is based on linear interpolation with parabolic blends (application of the trapezoidal velocity profile to the interpolation problem) for a path with via-points (Siciliano et al., 2008).

The path and control parameters are given in Tables 1 and 2. The control inputs (u_x, u_y) and (g_x, g_y) from the Lyapunov-based controller and NMPC, respectively, are shown in Fig. 5. The sampling rate was 100 Hz for the Lyapunov controller and 2.5 Hz for the NMPC.

The resulting velocity inputs $(\dot{x}_0, \dot{y}_0, \dot{z}_0, \dot{L})$ in (74)–(75) and (49) are shown in Fig. 4. The velocities in the horizontal plane, $\dot{x}_0$ and $\dot{y}_0$, were aggressive in the time interval $0 < t < 4.6$ s as a consequence of non-zero initial pendulum oscillations. After approximately 40 s, the velocity inputs $(\dot{x}_0, \dot{y}_0, \dot{z}_0, \dot{L})$ converged to zero. The actual (x_0, y_0, z_0, L) and desired (x_r, y_r, z_r, L_r) trajectories of the suspension point and cable length are illustrated in Fig. 6(a). The actual suspension point in the horizontal plane, x_0 and y_0, deviated from its reference in the time interval $0 < t < 11$ s as a consequence of non-zero initial pendulum oscillations. Otherwise, there were only small deviations between the actual and desired reference trajectories for the suspension point position and cable length. These deviations were mainly due to a time delay effect due to the sampling time τ of the nonlinear MPC controller, which lead to a slight delay between actual and desired trajectory. It is also worth noting that the commanded

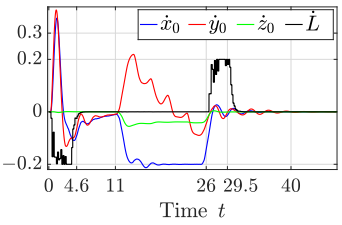

Fig. 4. The velocities $(\dot{x}_0, \dot{y}_0, \dot{z}_0, \dot{L})$ in (74)–(75) and (49) generated from the simulation study. The velocities are given in m/s.

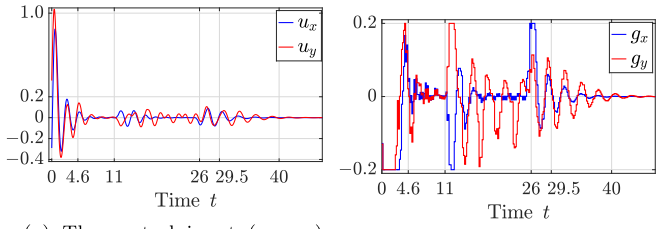

(a) The control input (u_x, u_y) from the Lyapunov-based controller.

(b) The control input (g_x, g_y) from the NMPC.

Fig. 5. The desired acceleration $\ddot{\boldsymbol{y}}^d$ of the crane tip in (23) from the simulation study. The control inputs are given in m/s^2.

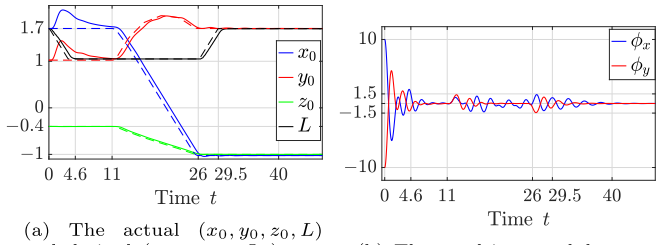

(a) The actual (x_0, y_0, z_0, L) and desired (x_r, y_r, z_r, L_r) trajectory given in m. The desired trajectory is represented as dashed lines.

(b) The resulting pendulum oscillation angles (ϕ_x, ϕ_y) given in deg.

Fig. 6. The pendulum oscillation angles and the actual and desired trajectories from the simulation study.

hoisting rate $\dot{L}$ and cable length L were kept within their bounds throughout the simulation study.

The pendulum oscillation angles (ϕ_x, ϕ_y) are illustrated in Fig. 6(b). After time $t = 4.6$ s, it is seen that the pendulum oscillations angles were bounded by $\pm 1.5°$ throughout the simulation study. Although the reference trajectory was non-stationary in the time interval $11 < t < 29.5$ s, the pendulum oscillation angles were still oscillating within $\pm 1.5°$. After time $t = 40$ s, the pendulum oscillation angles converged to zero due to stationary reference trajectory.

The simulation study demonstrated that the control system performed as intended with bounded pendulum oscillations while the suspension point and the cable length were tracking a desired reference trajectory.

6.2. Experimental validation

The performance of the proposed control system was further studied in experiments. The experimental setup was based on a specially designed scaled-down laboratory version of a knuckle boom crane with realistic geometry of the payload (Fig. 1(b)). The pendulum oscillation angles and rates were obtained by using a vision-based sensor system consisted of three consumer-grade web cameras, in combination with an extended Kalman filter. The crane was driven by one servo motor and two electro-mechanical cylinders (EMCs) driven by servo motors. All servo motors were equipped with encoders for measuring angles and angular velocities. Detailed explanation of the experimental setup is described in Tysse et al. (2021). The external control system of the test-bed was implemented using ROS (Robot Operating System) (Quigley et al., 2009) and the ROS Control framework (Chitta et al., 2017).

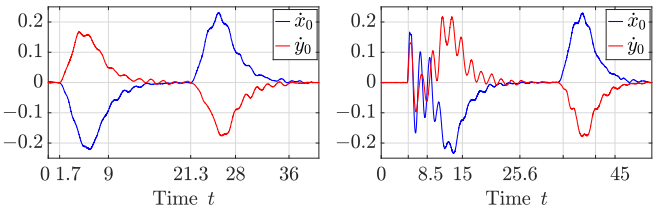

(a) Results from the study with zero initial pendulum oscillation angles.

(b) Results from the study with non-zero initial pendulum oscillation angles.

Fig. 7. The velocity $(\dot{x}_0, \dot{y}_0)$ in the horizontal plane given in (74) generated from the experimental study. The velocities are given in m/s.

In the experiment, the position reference for the crane tip was in the horizontal plane, and the control variables $(\dot{z}_0, \dot{L}) = (0, 0)$ were not used due to limited space and lack of winch. The experiment resembled a realistic hoisting operation where the reference trajectory (x_r, y_r) was represented as a slewing motion of 45° from an initial pick up site (x_i, y_i) to a landing site (x_f, y_f), then followed by a slewing motion of $-45°$ back to initial pick up site. The path and control parameters are given in Tables 1 and 2. The control inputs $\boldsymbol{u}$ and $\boldsymbol{w}$ from the Lyapunov-based controller and the NMPC, respectively, are shown in Figs. 10 and 11. The sampling rate was approximately 50 Hz for the Lyapunov controller and 2.5 Hz for the NMPC.

Two different initial pendulum oscillation cases were considered in the experiments. In the first run the initial conditions of the pendulum oscillation states were at the origin $(\phi_x, \phi_y, \dot{\phi}_x, \dot{\phi}_y) = (0, 0, 0, 0)$. In the second run the initial states were $(\phi_x, \phi_y, \dot{\phi}_x, \dot{\phi}_y) = (8°, -8°, 0, 0)$. The experiments demonstrated that the control system performed as planned with bounded pendulum oscillations, while the suspension point was tracking the reference trajectory in the horizontal plane. The practical application of the results indicates the potential of reducing risk and execution time in crane operations. In addition there could be potential of reducing stress on the crane structure and crane base which could arise from large pendulum oscillations of heavier payload.

6.3. Experiment with zero initial pendulum angles

An experimental study was performed with zero initial pendulum oscillation angles $(\phi_x, \phi_y) = (0, 0)$. The resulting commanded velocities $(\dot{x}_0, \dot{y}_0)$ in (74), are shown in Fig. 7(a). The velocities were zero until the starting time at 1.7 s of the trajectory, and converged to zero after 36 s. The commanded suspension point velocity $(\dot{x}_0, \dot{y}_0)$ in the horizontal plane was smooth throughout the experiment.

The actual (x_0, y_0) and desired (x_r, y_r) trajectory of the suspension point in the horizontal plane are illustrated in Fig. 8(a). As seen in the figure, the actual suspension point was close to the reference with a small time delay. Compared to the simulation study in Chapter 6, the experimental results had a larger time delay between the actual and desired suspension point position.

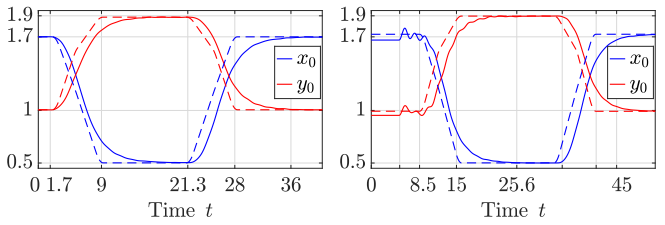

(a) Results from the study with zero initial pendulum oscillation angles.

(b) Results from the study with non-zero initial pendulum oscillation angles.

Fig. 8. The actual (x_0, y_0) and desired (x_r, y_r) suspension point trajectories in the horizontal plane generated from the experimental study. The desired trajectory is represented as dashed lines and the trajectories are given in m.

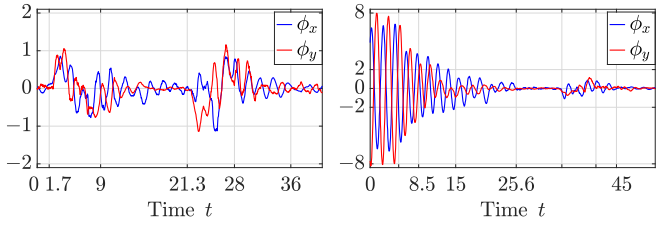

(a) Results from the study with zero initial pendulum oscillation angles.

(b) Results from the study with non-zero initial pendulum oscillation angles.

Fig. 9. The resulting pendulum oscillation angles (ϕ_x, ϕ_y) generated from the experimental study. The angles are given in deg.

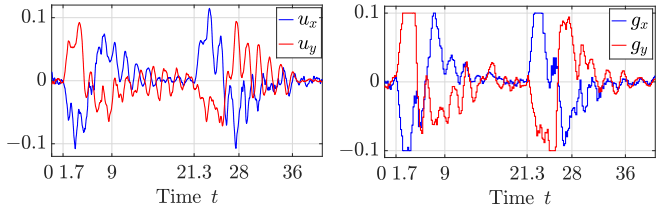

(a) The control input $\boldsymbol{u}$ from the Lyapunov-based controller.

(b) The control input $\boldsymbol{w}$ from the NMPC.

Fig. 10. The desired acceleration $\ddot{\boldsymbol{y}}^d$ of the crane tip in (23) from the experimental study with zero initial pendulum oscillation angles. The control inputs are given in m/s^2.

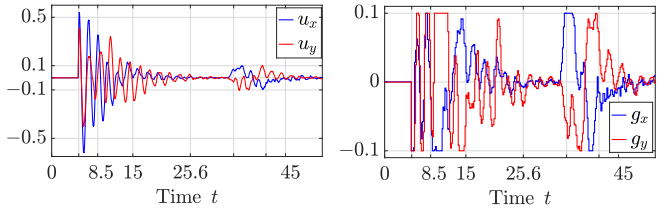

(a) The control input $\boldsymbol{u}$ from the Lyapunov-based controller.

(b) The control input $\boldsymbol{w}$ from the NMPC.

Fig. 11. The desired acceleration $\ddot{\boldsymbol{y}}^d$ of the crane tip in (23) from the experimental study with non-zero initial pendulum oscillation angles. The control inputs are given in m/s^2.

The reason for this is the time delay in the communication and the slower response of the knuckle boom crane.

The resulting pendulum angles (ϕ_x, ϕ_y) are shown in Fig. 9(a). The pendulum angles were zero until the starting time 1.7 s of the commanded motion, and converged to zero after t =36 s. In the time interval $1.7 < t < 28$ s, the pendulum angles were oscillating because the suspension point was following a moving trajectory in this interval. Throughout the experiment, the pendulum angles were limited to $\pm 2°$.

6.4. Experiment with non-zero initial pendulum angles

An experiment was performed with initial pendulum angles $(\phi_x, \phi_y) \approx (8°, -8°)$. The commanded velocities $(\dot{x}_0, \dot{y}_0)$ in (74), are shown in Fig. 7(b). Compared to the velocity in Section 6.3, the velocity in this case was oscillating in the interval $0 < t < 25$ s due to the non-zero initial pendulum angles. In the time interval $t > 25$ s the velocities in both experimental studies were approximately the same.

The actual (x_0, y_0) and desired (x_r, y_r) trajectories of the suspension point are illustrated in Fig. 8(b). Compared to the trajectory (x_0, y_0) in Section 6.3, the trajectory in this case was deviating from the reference in the interval $0 < t < 8.5$ s due to initial pendulum rotations which caused the control variables (u_x, u_y) to be more dominating than the perturbations (g_x, g_y). In the time interval $t > 8.5$ s the trajectories in both studies were approximately the same.

The resulting pendulum angles are shown in Fig. 9(b). The pendulum was oscillating with angles less than $\pm 2°$ after 15 s. After 15 s the pendulum rotations in both experimental studies were approximately the same, and converged to zero after 45 s. It is worth noting that the pendulum angles were damped out slower than in the simulation in Chapter 6 due to time delay in the communication and slower response of the knuckle boom crane.

7. Conclusions

A controller has been designed for the control of the crane payload position using a Lyapunov-based pendulum damping controller which stabilizes the pendulum dynamics, and an NMPC position controller which is designed for the stabilized dynamics. The Lyapunov-based controller was designed to be exponentially stable, so that the pendulum motion state would be ultimately bounded in the presence of bounded perturbations. Then the position of the crane tip and cable length were controlled using NMPC where the control variables appear as the bounded perturbations for the Lyapunov-based controller, which made it possible to constrain the perturbations by constraining the control variables of the NMPC. The performance of the controller was demonstrated in a simulation study and in experiments. The simulated operation was conducted by first lifting the payload by decreasing the cable length, then followed by a movement of the suspension point by a circular helix motion of 90° with radius 2 m and pitch -2.4 m rad^{-1}, and at last the payload was lowered by increasing the cable length. The experimental operation was conducted by a slewing motion of 45°, then followed by a slewing motion of $-45°$ back to the initial position. The radius of the slewing motion was 2 m. Both the simulated and experimental operation was executed in approximately 30 s. In the simulation, the pendulum oscillation angles were bounded within $\pm 1.5°$ while the suspension point and cable length were following a reference trajectory. The pendulum motions converged to zero when the crane tip and cable length reached their final static desired reference. In the experiments the pendulum oscillation angles were bounded within $\pm 2°$ after 15 s and while the suspension point was following a reference trajectory. The pendulum motions converged to zero when the crane tip reached its final static desired reference.

References

Abdel-Rahman, E. M., Nayfeh, A. H., & Masoud, Z. N. (2003). Dynamics and control of cranes: A review. *Modal Analysis*, *9*(7), 863–908.

Andersson, J. A. E., Gillis, J., Horn, G., Rawlings, J. B., & Diehl, M. (2019). CasADi – A software framework for nonlinear optimization and optimal control. *Mathematical Programming Computation*, *11*(1), 1–36.

Arnold, E., Sawodny, O., Neupert, J., & Schneider, K. (2005). Anti-sway system for boom cranes based on a model predictive control approach. In *IEEE international conference on mechatronics and automation* (pp. 1533–1538).

Blackburn, D., Lawrence, J., Danielson, J., Singhose, W., Kamoi, T., & Taura, A. (2010). Radial-motion assisted command shapers for nonlinear tower crane rotational slewing. *Control Engineering Practice*, *18*(5), 523–531.

Chitta, S., Marder-Eppstein, E., Meeussen, W., Pradeep, V., Rodríguez Tsouroukdissian, A., Bohren, J., Coleman, D., Magyar, B., Raiola, G., Lüdtke, M., & Fernández Perdomo, E. (2017). ros_control: A generic and simple control framework for ROS. *The Journal of Open Source Software*, *2*.

Chung, C. C., & Hauser, J. (1995). Nonlinear control of a swinging pendulum. *Automatica*, *31*, 851–862.

Cibicik, A., Myhre, T. A., & Egeland, O. (2018). Modeling and control of a bifilar crane payload. In *Proceedings 2018 American control conference (ACC)* (pp. 1305–1312).

Cutforth, C. F., & Pao, L. Y. (2004). Adaptive input shaping for maneuvering flexible structures. *Automatica*, *40*(4), 685–693.

Fang, Y., Zergeroglu, E., Dixon, W. E., & Dawson, D. M. (2001). Nonlinear coupling control laws for an overhead crane system. In *Proceedings of the 2001 IEEE international conference on control applications (CCA'01)* (pp. 639–644).

Findeisen, R., & Allgöwer, F. (2002). An introduction to nonlinear model predictive control. In *21st Benelux meeting on systems and control, Veidhoven* (pp. 1–23).

Golub, G. H., & Van Loan, C. F. (1996). *Matrix computations* (3rd ed.). Baltimore, MD, USA: Johns Hopkins University Press.

Grüne, L., & Pannek, J. (2013). *Nonlinear model predictive control: Theory and algorithms*. Springer.

Kane, T. R., & Levinson, D. A. (1985). *Dynamics: Theory and applications*. McGraw-Hill.

Khalil, H. (2002). *Pearson education*, *Nonlinear systems*. Prentice Hall.

Kimiaghalam, B., Homaifar, A., & Sayarrodsari, B. (2001). An application of model predictive control for a shipboard crane. *2*, In *Proceedings 2001 American control conference (ACC)* (pp. 929–934).

Knierim, K. L., Krieger, K., & Sawodny, O. (2010). Flatness based control of a 3-DOF overhead crane with velocity controlled drives. *43*, In *IFAC Proceedings* (pp. 363—368).

Kolar, B., Rams, H., & Schlacher, K. (2017). Time-optimal flatness based control of a gantry crane. *Control Engineering Practice*, *60*, 18–27.

Mayne, D., Rawlings, J., Rao, C., & Scokaert, P. (2000). Constrained model predictive control: Stability and optimality. *Automatica*, *36*(6), 789–814.

Mills, A., Wills, A., & Ninness, B. (2009). Nonlinear model predictive control of an inverted pendulum. In *Proceedings 2009 American control conference (ACC)* (pp. 2335–2340).

Neupert, J., Arnold, E., Schneider, K., & Sawodny, O. (2010). Tracking and anti-sway control for boom cranes. *Control Engineering Practice*, *18*(1), 31–44.

Qian, Y., Fang, Y., & Lu, B. (2017). Adaptive repetitive learning control for an offshore boom crane. *Automatica*, *82*, 21–28.

Quigley, M., Gerkey, B., Conley, K., Faust, J., Foote, T., Leibs, J., Berger, E., Wheeler, R., & Ng, A. (2009). ROS: An open-source robot operating system. In *Proc. of the IEEE intl. conf. on robotics and automation (ICRA) workshop on open source robotics*. Kobe, Japan.

Ramli, L., Mohamed, Z., Abdullahi, A. M., Jaafar, H., & Lazim, I. M. (2017). Control strategies for crane systems: A comprehensive review. *Mechanical Systems and Signal Processing*, *95*(C), 1–23.

Rauscher, F., Nann, S., & Sawodny, O. (2018). Motion control of an overhead crane using a wireless hook mounted IMU. In *Proceedings 2018 american control conference (ACC)* (pp. 5677–5682). IEEE.

Sakawa, Y., & Nakazumi, A. (1985). Modeling and control of a rotary crane. *Journal of Dynamic Systems, Measurement, and Control*, *107*(3), 200–206.

Shkolnik, A., & Tedrake, R. (2008). High-dimensional underactuated motion planning via task space control. In *Proceedings of 2008 IEEE/RSJ international conference on intelligent robots and systems* (pp. 3762–3768).

Siciliano, B., Sciavicco, L., Villani, L., & Oriolo, G. (2008). *Robotics: Modelling, planning and control* (1st ed.). Springer Publishing Company, Incorporated.

Smoczek, J., & Szpytko, J. (2017). Particle swarm optimization-based multivariable generalized predictive control for an overhead crane. *IEEE/ASME Transactions on Mechatronics*, *22*(1), 258–268.

Spong, M. (1994). Partial feedback linearization of underactuated mechanical systems. In *Proceedings of IEEE/RSJ international conference on intelligent robots and systems (IROS'94), vol. 1* (pp. 314–321).

Sun, N., Fang, Y., Chen, H., & He, B. (2015). Adaptive nonlinear crane control with load hoisting/lowering and unknown parameters: Design and experiments. *IEEE/ASME Transactions on Mechatronics*, *20*(5), 2107–2119.

Sun, N., Fang, Y., Chen, H., Lu, B., & Fu, Y. (2016). Slew/translation positioning and swing suppression for 4-DOF tower cranes with parametric uncertainties: Design and hardware experimentation. *IEEE Transactions on Industrial Electronics*, *63*(10), 6407–6418.

Sun, N., Fang, Y., & Zhang, X. (2013). Energy coupling output feedback control of 4-DOF underactuated cranes with saturated inputs. *Automatica*, *49*(5), 1318–1325.

Tysse, G. O., Cibicik, A., & Egeland, O. (2021). Vision-based control of a knuckle boom crane with online cable length estimation. *IEEE/ASME Transactions on Mechatronics*, *26*(1), 416–426.

Tysse, G. O., & Egeland, O. (2019). Crane load position control using Lyapunov-based pendulum damping and nonlinear MPC position control. In *18th European control conference* (pp. 1628–1635).

Vukov, M., Loock, W. V., Houska, B., Ferreau, H., Swevers, J., & Diehl, M. (2012). Experimental validation of nonlinear MPC on an overhead crane using automatic code generation. In *Proceedings 2012 American control conference (ACC)* (pp. 6264–6269).

Wächter, A., & Biegler, L. T. (2006). On the implementation of an interior-point filter line-search algorithm for large-scale nonlinear programming. *Mathematical Programming*, *106*, 25–57.

Wen, J. T., & Bayard, D. (1988). A new class of control laws for robotic manipulators - Part I: Non-adaptive case. *International Journal of Control*, *47*(5), 1361–1385.

Wu, X., & He, X. (2016). Partial feedback linearization control for 3-D underactuated overhead crane systems. *ISA Transactions*, *65*, 361–370.

Wu, Z., Xia, X., & Zhu, B. (2015). Model predictive control for improving operational efficiency of overhead cranes. *Nonlinear Dynamics*, *79*(4), 2639–2657.

Yoshida, K. (1998). Nonlinear controller design for a crane system with state constraints. In *Proceedings of the 1998 American control conference (ACC)* (pp. 1277–1283).

Yu, J., Lewis, F. L., & Huang, T. (1995). Nonlinear feedback control of a gantry crane. In *Proceedings 1995 American control conference (ACC)* (pp. 4310–4315).

Geir Ole Tysse received the M.Sc. degree in subsea technology from the Norwegian University of Science and Technology (NTNU), Trondheim, Norway, in 2015. He received the Ph.D. degree in mechanical and industrial engineering from the Norwegian University of Science and Technology (NTNU), Trondheim, Norway, in 2020. His research interests include vision and estimation theory, robotics, control systems, mathematical modeling of rigid multibody systems and dynamics of marine vessels.

Andrej Cibicik received the M.Sc. degree in civil engineering from the Technical University of Denmark (DTU), Copenhagen, in 2012. He received the Ph.D degree in mechanical and industrial engineering from the Norwegian University of Science and Technology (NTNU), Trondheim, Norway, in 2020. From 2012 to 2016 he held industrial positions within structural strength analysis of civil structures and offshore drilling equipment. Currently he is a research scientist at the Dept. of Production Technology in SINTEF Manufacturing, Trondheim, Norway. His research interests include robotics, multibody dynamics, automatic control, sensor systems and estimation.

Lars Tingelstad received the M.Sc. and Ph.D. degree in Mechanical Engineering from the Norwegian University of Science and Technology, NTNU, in 2011 and 2017, respectively. His Ph.D. thesis was on the estimation of rigid body motions from observations of 3-D geometric objects such as points, lines, planes, circles, and spheres, in conformal geometric algebra. He is currently Associate Professor of robotic production at NTNU. His research interests are within computer vision and robotic production, in general, and within constraint-based methods in robotic assembly, in particular.

Olav Egeland received the M.Sc. and Ph.D. degrees in automatic control from the Norwegian University of Science and Technology (NTNU), Trondheim, Norway, in 1984 and 1987. He was Professor of automatic control at NTNU from 1989 to 2004, and worked as co-founder of a start-up from 2004 to 2011. He is currently Professor of production automation at NTNU. His research interests are within mathematical modeling, robotic production, and offshore control systems. Dr. Egeland received the Automatica Prize Paper Award in 1996 and the IEEE Transactions on Control System Technology Outstanding Paper Award in 2000. He was an Associate Editor of the IEEE Transactions on Automatic Control from 1996 to 1999 and the European Journal of Control from 1998 to 2000.